

Spiral Imaging: A Critical Appraisal

Kai Tobias Block, MSc and Jens Frahm, PhD*

In view of recent applications in cardiovascular and functional brain imaging, this work revisits the basic performance characteristics of spiral imaging in direct comparison to echo-planar imaging (EPI) and conventional rapid gradient-echo imaging. Using both computer simulations and experiments on phantoms and human subjects at 2.9 T, the study emphasizes single-shot applications and addresses the design of a suitable trajectory, the choice of a gridding algorithm, and the sensitivity to experimental inadequacies. As a general result, the combination of a spiral trajectory with regridding of the k-space data poses no principle obstacle for high-quality imaging. On the other hand, experimental difficulties such as gradient deviations, resonance offset contributions, and concomitant field effects cause more pronounced and even less acceptable image artifacts than usually obtained for EPI. Moreover, when ignoring parallel imaging strategies that are also applicable to EPI, improvements of image quality via reduced acquisition periods are only achievable by interleaved multishot spirals because partial Fourier sampling and rectangular fields of view (FOVs) cannot be exploited for non-Cartesian trajectories. Taken together, while spiral imaging may find its niche applications, most high-speed imaging needs are more easily served by EPI.

Key Words: magnetic resonance imaging; echo-planar imaging; single-shot imaging; spiral imaging; regridding

J. Magn. Reson. Imaging 2005;21:657–668.

© 2005 Wiley-Liss, Inc.

ALTHOUGH SPIRAL SCANNING TRAJECTORIES have been known since the early days of rapid scan magnetic resonance imaging (MRI), spiral imaging never became a widely accepted and clinically used method. More recently, however, based on significant hardware improvements in the development of flexible gradient systems, spiral scanning has regained interest with applications in cardiovascular and functional brain imaging. Due to its ability to acquire the k-space data of a two-dimensional image after only a single radio frequency (RF) excitation, single-shot spiral imaging emerges as a competing technique to echo-planar imaging (EPI).

In principle, spiral trajectories offer some inherent refocusing of motion- and flow-induced phase errors (1–3) not delivered by conventional phase- and frequency-encoding gradients, that is Cartesian trajectories that scan the k-space along straight lines. Furthermore, spiral trajectories allow for an efficient and temporally flexible sampling of k-space as shorter pathways are required to cover a desired region and the data acquisition may start in the center of k-space. These advantages are counterbalanced by practical difficulties that—at least in the eyes of a typical MRI user—render spiral imaging a technical challenge that seems to be better suited for a few expert users. It is therefore the primary aim of this article to provide a comprehensive review of the basic performance characteristics of (single-shot) spiral imaging in direct comparison with EPI. Furthermore, the analysis attempts to sort out whether spiral imaging suffers problems of a principle nature other than EPI or whether existing complications represent mere difficulties that are to be overcome by improved algorithms, foreseeable computer speed, and more user-friendly implementations.

In more detail, this work addresses three major areas that differ from conventional scanning schemes: 1) the calculation of the gradient waveforms for spatial encoding with respect to limitations given by the sampling theorem and gradient hardware, 2) the interpolation or regridding of the k-space data before image reconstruction by a two-dimensional fast Fourier transform (FFT), and 3) the nature and potential correction of artifacts in spiral images. The investigations employed both numerical simulations and experimental assessments at 3 T in phantoms and humans focusing on brain imaging. The combination of simulated and experimental data turned out to be essential for the identification of artifact sources and the desired separation of basic and temporary problems.

All measurements were conducted at 2.9 T (Siemens Magnetom Trio, Erlangen, Germany) using a transmit/receive head coil (USA Instruments, Aurora, OH, USA) and 40 mT m⁻¹ gradients with a maximum slew rate of 200 mT m⁻¹ msec⁻¹. Written informed consent was obtained from all subjects prior to the examination. Calculations including gradient waveforms, image reconstruction, and simulations were performed offline with software modules written in Visual C++ (Version 6.0, Microsoft Corporation, Redmond, WA, USA) using the GNU Scientific Library. Unless stated otherwise, all images correspond to a resolution of 128 × 128 pixels

Biomedizinische NMR Forschungs GmbH am Max-Planck-Institut für biophysikalische Chemie, Göttingen, Germany.

*Address reprint requests to: J.F., Biomedizinische NMR Forschungs GmbH, 37070 Göttingen, Germany. E-mail: jfracm@gwdg.de

Received October 13, 2004; Accepted February 17, 2005.

DOI 10.1002/jmri.20320

Published online in Wiley InterScience (www.interscience.wiley.com).

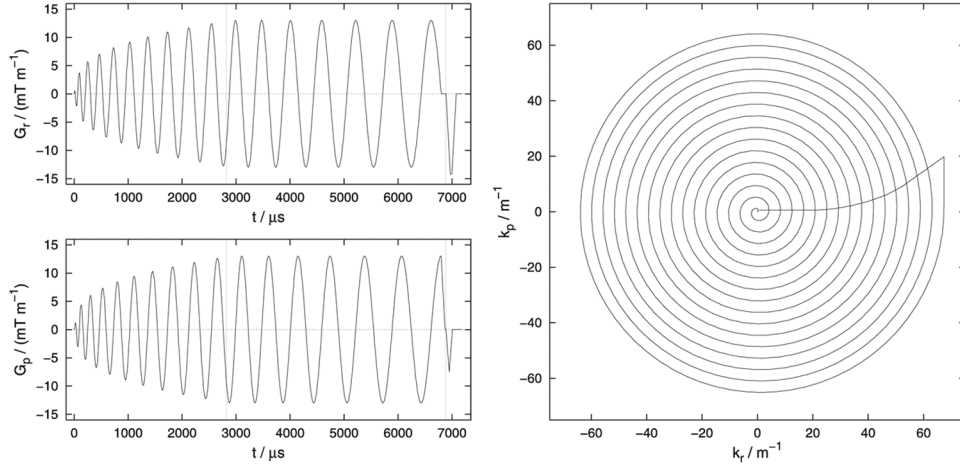


Figure 1. Gradient waveforms calculated according to the analytical approximation proposed by Glover (7) and corresponding spiral trajectory. For details, see text.

covering a 24-cm quadratic field of view (FOV). Simulations were done by evaluating the analytical Fourier transform of well-known simulation objects as a function of the given gradient waveforms. Numerical phantoms were composed of different ellipses such as the Shepp-Logan phantom (4), in which case the analytical Fourier transform is a simple superposition of Bessel functions.

TRAJECTORY DESIGN

Theory

Although different realizations are possible, most spiral imaging sequences rely on Archimedean spirals, i.e., spiral trajectories with equidistant revolutions. An Archimedean spiral can be parameterized by

$$\mathbf{k}(t) = \alpha \cdot \theta(t) \cdot e^{i\theta(t)} \quad (1)$$

where $\theta(t)$ represents a monotonically increasing function and $\mathbf{k}(t) = k_x(t) + i \cdot k_y(t)$. In order to fulfill the sampling theorem for a given FOV, the distance between neighboring revolutions is chosen as $\Delta k = 1/\text{FOV}$. The trajectory in k-space is given by the time integral of the gradient waveform $\mathbf{G}(t)$. Therefore, the required gradients for a given trajectory can be calculated by

$$\mathbf{G}(t) = \frac{1}{\gamma} \cdot \frac{d}{dt} \mathbf{k}(t) \quad (2)$$

which for a spiral trajectory as given by Eq. [1] yields

$$\mathbf{G}(t) = \frac{\alpha}{\gamma} \cdot \dot{\theta}(t) \cdot [1 + i\theta(t)] \cdot e^{i\theta(t)}. \quad (3)$$

The function $\theta(t)$ defines the distribution of sample points along the spiral trajectory. It has to be chosen with particular care as the gradient waveforms have to comply with the hardware limitations (gradient amplitude, slew rate), while simultaneously the trajectory

should provide for a most uniform and fast sampling of k-space. The intuitive choice of a linear function for $\theta(t)$ would result in an unfavorable spiral with constant angular speed that spends too much time in the central part of the spiral, i.e., for revolutions with small radii. On the other hand, a square root dependence according to $\theta(t) = \sqrt{t}$ would lead to an approximately constant orbit speed for large t . Although this is a desirable feature, the function causes a singularity at $t = 0$ from $d\theta/dt$, which renders this solution unusable. As a consequence, the optimization of $\theta(t)$ in between the two aforementioned cases remains a persistent challenge for the gradient calculation in spiral imaging.

A practical solution proposed by Börner et al (5) is

$$\theta(t) = \frac{t}{\sqrt{\alpha + (1 - \alpha) \cdot t}}, \quad (4)$$

where the parameter α may be used to tune the spiral between constant angular speed and constant orbit speed. A more accurate solution for the calculation of the gradient waveforms may be obtained by formulating the problem as a differential equation with suitable boundary conditions (6). Unfortunately, however, an analytical solution to this equation has not been found, and because the numerical solution requires a high computational load, it needs to be performed offline. A simple analytical approximation to the differential equation has been presented by Glover (7) and shown to adequately reproduce the exact solution. The approach first increases the gradient amplitude until its maximum value (slew-rate-limited case) and then keeps the amplitude constant (amplitude-limited case). In either case, the slope of the waveform, which is dominated by the rotation frequency of the trajectory, has to comply with the slew-rate limitation of the gradient system. Figure 1 shows the gradient waveforms calculated with this algorithm together with the resulting trajectory.

Corresponding multishot trajectories may be obtained by increasing the revolution distance from Δk to $n \cdot \Delta k$ and rotating the individual trajectories by $\phi =$

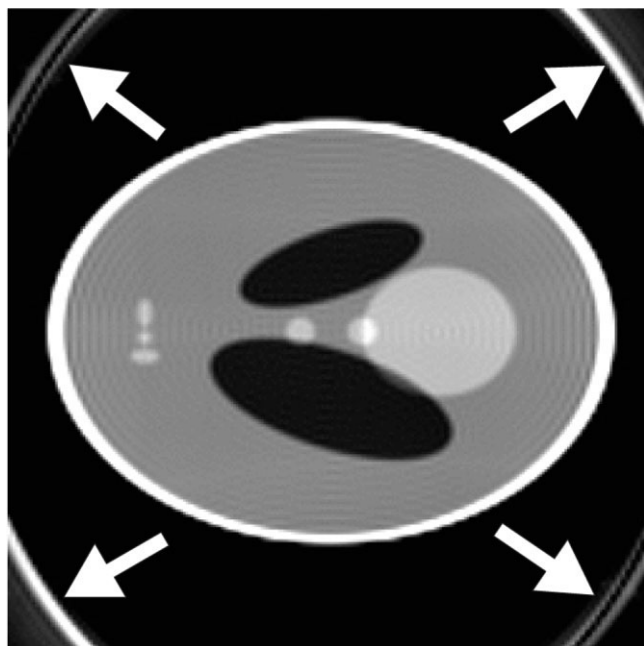


Figure 2. Simulated spiral image (128×128 matrix) of a numerical phantom using the gradient waveforms and trajectory shown in Fig. 1.

$2\pi/n$ for each of the n excitations. A combination of the sampled data from all excitations, i.e., from all interleaved spiral trajectories, yields a sample density comparable to that of a single-shot scan with extended acquisition period. Of course, the minimum length of the acquisition period of a multishot spiral decreases with the number of excitations at the expense of overall scan time.

Simulations

The performances in terms of achievable image quality of the Börner et al (5) and Glover (7) algorithms for calculating spiral trajectories were evaluated using numerical simulations. It turns out that both methods yield satisfactory results by delivering a suitable reproduction of the simulation object with almost identical artifacts. Because the respective images are indeed indistinguishable by visual inspection, Fig. 2 demonstrates for the case of the Glover algorithm that the residual artifacts in the image edges do not affect the object itself (although they may cause aliasing if the object extends the FOV). They most likely result from a partial violation of the sampling theorem as a reduction of the revolution distance shifts the effects further away from the object. This also indicates that pertinent artifacts may not be ascribed to regridding problems as occasionally suggested.

Summary

Because the two aforementioned algorithms for calculating spiral gradient waveforms differ in the time needed to sample the k-space, all subsequent investigations were performed with the more efficient solution by Glover, which best exploits the available gradient

amplitude and slew rate. Apart from reducing the measurement time for single-shot imaging, a shorter acquisition time due to a faster scanning of k-space reduces the degree of signal dephasing in the presence of magnetic field inhomogeneities. In fact, though theoretically possible, a further improvement of the existing approximate algorithm is not expected to translate into better image quality in view of other experimental problems (see below). The present approaches for calculating spiral gradient trajectories are certainly not the limiting factor for practical applications of spiral imaging.

It should be noted that, in contrast to spiral imaging, EPI offers an additional decrease of the acquisition time by partial Fourier imaging and the use of a non-square FOV. Due to the coupled waveforms of both encoding gradients in spiral imaging, partial Fourier techniques cannot directly be adapted, while a one-dimensional reduction of k-space does not automatically lead to faster scanning.

IMAGE RECONSTRUCTION

Despite a tremendous increase of computational speed during recent years, very long reconstruction times still preclude a direct discrete Fourier transformation of spiral (or other nonuniformly sampled) k-space data for routine imaging. On the other hand, the use of an FFT requires equally spaced data points on a rectangular grid, which is obviously not fulfilled for spiral trajectories, as shown in Fig. 3. The only practicable solution is an interpolation of the acquired data onto a rectangular grid in a target matrix followed by FFT for image reconstruction.

The regridding of the original data is a nontrivial enterprise because any interpolation in the frequency domain represents a convolution of the data with a kernel function. Due to the properties of the Fourier transformation, this convolution corresponds to a multiplication of the data in the image domain with the Fourier transform of the kernel. As a consequence, for example, the simple choice of a linear interpolation in the frequency domain would lead to an unfortunate multiplication of the image with a squared sinc function. A second problem arises from the fact that spiral trajectories provide an inhomogeneous coverage of k-space and thus cause a variable density of sampling points. This property has to be compensated for in order to avoid an overweighting of low spatial frequencies and corresponding intensity distortions and image blurring.

The following sections summarize the results for the major regridding and respective density compensation techniques. In order to facilitate the comparison of the achievable image quality, Fig. 4 focuses on only a few selected results from the extensive simulations of spiral images, which were obtained for three different reconstruction methods.

Augmented Matrix Method

The simplest approach to the gridding problem is to increase the number of grid points in the target matrix (8). The procedure decreases the mean distance be-

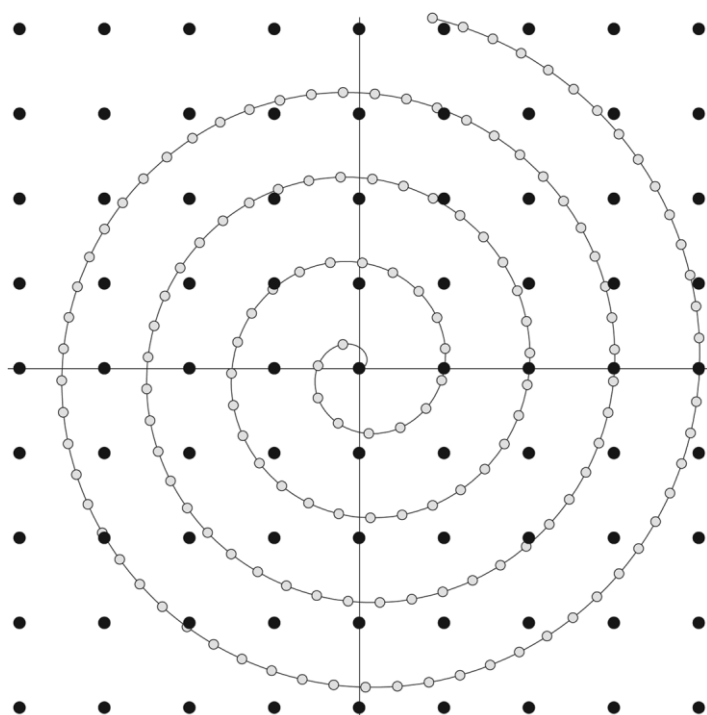


Figure 3. Arrangement of data points in k-space for a spiral trajectory (open circles) and a rectangular grid (solid circles) as obtained for conventional spin-warp scanning.

tween the acquired data points along the spiral trajectory and the desired rectangular grid. Of course, the higher density of the grid results in a virtual increase of the FOV, which can be restored by removing the unnecessary border regions after FFT. For this method, a simple solution to the density compensation problem is to weight each grid point with the number of spiral trajectory points in its (immediate) neighborhood.

Figure 4 (top row) compares simulated spiral images that were reconstructed by the augmented matrix method using a twofold (left) and fivefold (right) increase of a matrix, which would correspond to a rectangular acquisition with the same nominal resolution. The images suffer from patterned artifacts, which decrease in strength for larger matrices. On the other hand, for the fivefold matrix size, the spiral image is compromised by a homogeneous blurring that is best appreciated by the smearing of intensities that covers the black ellipses of the numerical phantom. This effect is not a general feature of the augmented matrix method but reflects a failure of the simple density compensation for large matrices when the average number of original data points assigned to a grid point in the target matrix approaches 1. Most recently, however, a significantly improved approach has been proposed by Moriguchi and Duerk (9). The idea promises to overcome some of the aforementioned limitations by a combination of the augmented matrix method with an iterative reconstruction scheme based on a variant of the projection onto convex sets (POCS) optimization method (10,11).

Conventional Regridding

So far, the most widely used gridding method has been introduced by O'Sullivan (12) for computed tomography—here referred to as conventional regridding. The underlying idea is that an optimal interpolation in the

frequency domain would be a convolution of the measured data with a sinc function. Because its Fourier transform is a boxcar function, the sinc interpolation would not affect the image after FFT. For practical purposes, it is inevitable to use a truncated and filtered sinc interpolation kernel that not only avoids arrays of infinite size, but also speeds up the computation by reducing the number of floating-point operations. Based on a comparison of different window functions with respect to resulting image quality, Jackson et al (13) suggested a Kaiser-Bessel window, which was also applied here. It should be noted that a truncated sinc or any other window function results in intensity distortions in the image. The effect must be dealt with after reconstruction by a procedure called roll-off correction, which divides the local image intensity by the Fourier transform of the kernel. A further reduction of interpolation artifacts may be achieved by adding the augmented matrix method and doubling the number of data points (also referred to as oversampling).

Prior to convolution of the measured data, it is necessary to perform a suitable density compensation. Among several possible methods, Meyer et al (14) suggested an analytical solution, which is specifically tailored to spiral trajectories but not applicable to modified spiral or even arbitrary trajectories. A more general solution can be realized using Voronoi diagrams (15), which determine the size of the area surrounding each trajectory point by a geometrical algorithm and then apply this measure to weight the local sample points.

As demonstrated by the simulations shown in Fig. 4 (middle row), conventional regridding using a convolution with a Kaiser-Bessel function allows for a reconstruction of high-quality spiral images. This particularly applies to reconstructions that complement the standard approach (left) by a twofold increase of the

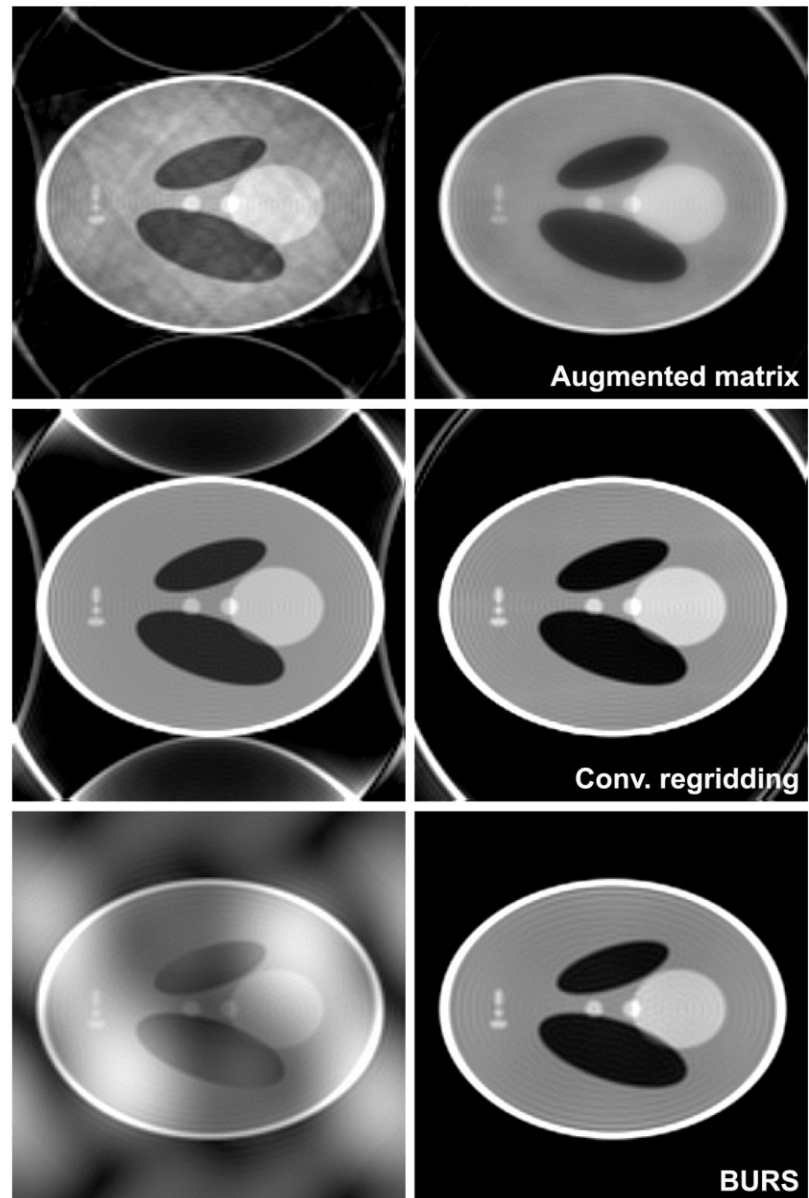


Figure 4. Image reconstruction methods. Simulations of spiral images (numerical phantom as in Fig. 1) obtained by the augmented matrix method (top), by conventional regridding (middle), and by the BURS method (bottom) (96×96 matrix). The examples for the augmented matrix method represent a twofold (left) and a fivefold (right) increase of the matrix size. Conventional regridding was used without (left) and with (right) twofold oversampling as the standard approach. The BURS method was applied with suboptimal (left) and optimal (right) parameters. For further details, see text.

data matrix (right). In more detail, the accuracy of the reproduced intensity profiles of the numerical phantom depends not only on the chosen kernel, but also on the density compensation. Here, no visible differences were obtained for either the analytical density compensation (14) or the use of Voronoi diagrams (15). In terms of practical applicability, the analytical density compensation offers fast and robust processing, whereas the Voronoi approach allows for flexibility of the trajectory design at the expense of high computational requirements. If only a single set of gradients is needed for routine applications, this latter problem may be circumvented by a precalculation and storage of the coefficients for the density correction in a lookup table.

Block Uniform Resampling

The block uniform resampling (BURS) algorithm (16) represents a class of methods that are based on a backward formulation of the gridding problem. In this case,

regridding—as the forward process—is achieved by a numerical inversion of the interpolation step essential to the backward operation: suppose one knows the (desired) data values at the positions of a rectangular grid, then it is possible to calculate the (measured) values at the trajectory positions using a sinc interpolation. In this backward calculation, a density compensation is not needed because the sampling density of the grid is homogeneous. The actual interpolation of the backward operation involves a multiplication of the vector of the (desired) data values with an interpolation matrix, which can be derived from the trajectory and grid positions using the sinc function. The procedure yields a new vector that contains the (measured) data values at the trajectory positions. To solve the gridding problem, the whole process may be reversed: if one inverts the interpolation matrix determined for the backward calculation, then the (desired) values at the grid positions may be obtained by multiplying the (measured) data

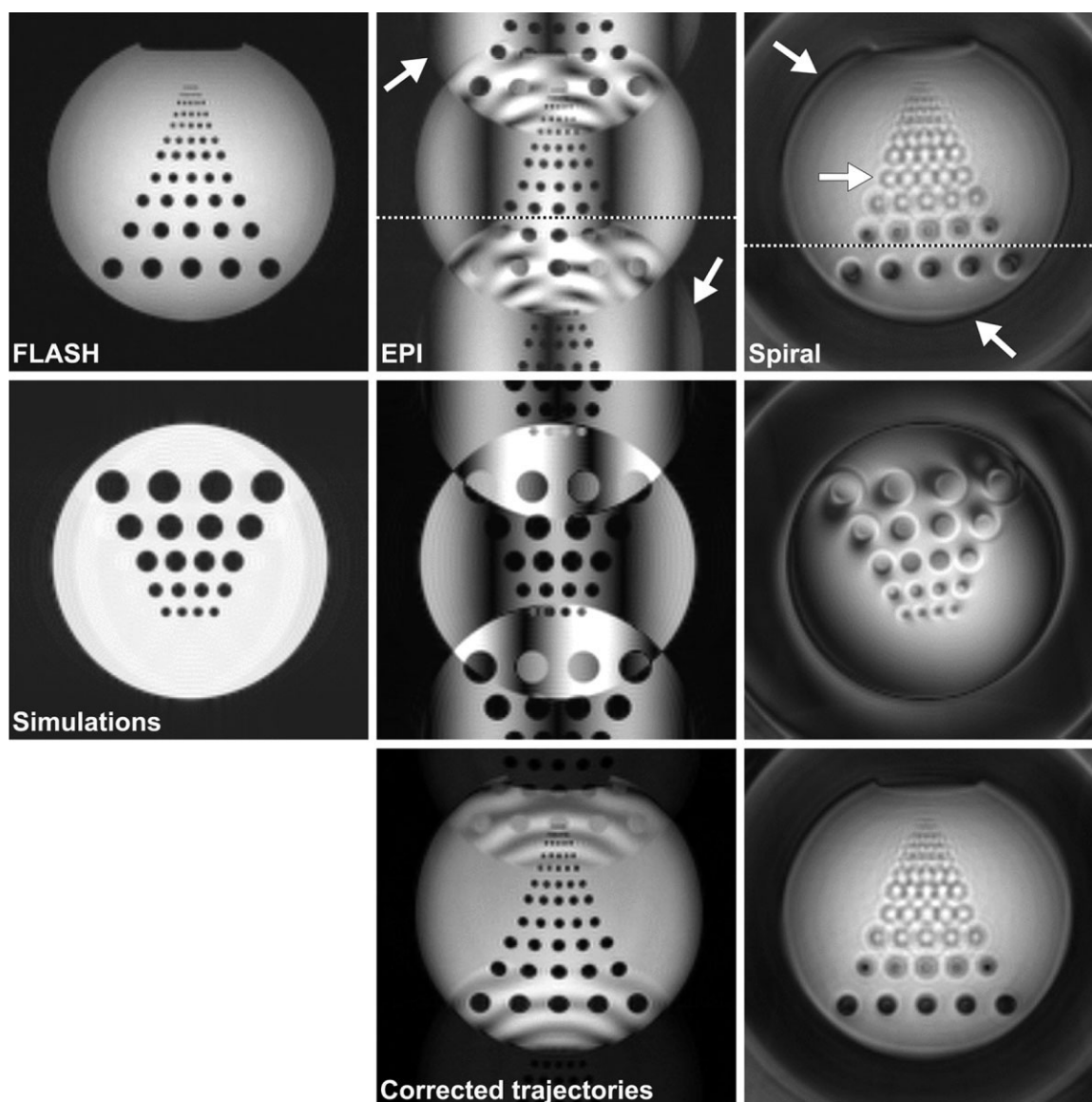


Figure 5. Experimental artifacts in FLASH, EPI, and spiral image acquisitions of a standard quality assurance phantom. Top: Experimental images at 2.9 T without corrections for the actual trajectory cause artifacts (arrows) such as ghosting for EPI and blurring for spiral acquisitions. Middle: Simulated images of a numerical phantom. The results were obtained by using the theoretical trajectory for reconstructing data from a modeled (distorted) trajectory and indicate a major portion of the artifacts to originate from gradient deviations. Bottom: Experimental images based on corrected (time-shifted) EPI and spiral trajectories according to the gradient waveforms shown in Fig. 6.

vector of the original trajectory positions with the inverse matrix.

Technically, the inversion of the interpolation matrix is done numerically using singular value decomposition (17). Because its large size precludes an inversion of the matrix as a whole, a practicable solution is to perform the inversion locally within the regional neighborhood of each grid point. As a consequence, the lower number of grid and trajectory points in the inversion reduces the optimality of the numerical solution, which is at the expense of image quality. For practical implementations, the size of the neighborhood needs to be carefully tuned for both grid points and trajectory points. If this can be accomplished, for example, as shown for the simulated image in Fig. 4 (bottom right), then also the

BURS method yields a suitable reconstruction of spiral images with correct intensity profiles. In general, however, the achievable image quality critically depends on the chosen parameters. Figure 4 (bottom left) demonstrates that the related intensity distortions may easily render a BURS-reconstructed spiral image useless.

Such sensitivities and image artifacts most likely result from unstable solutions to the ill-posed inverse problem (18). The corresponding errors are particularly strong when the number of trajectory points equals the number of grid points. As a consequence, certain areas of the trajectory are more affected than others due to the varying sampling density, so that perturbations in specific frequency regions result in respective image distortions. It has been proposed to stabilize the BURS

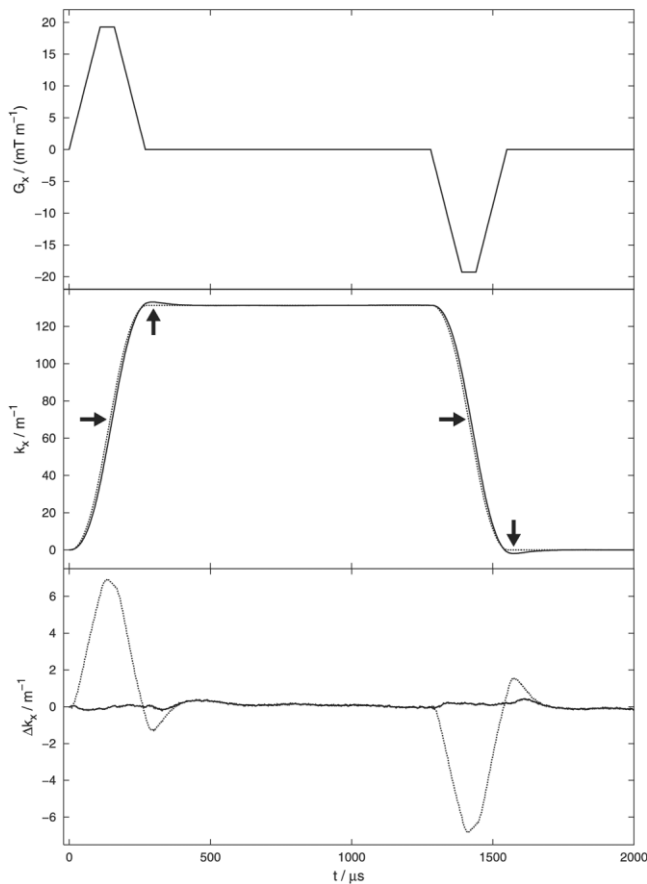


Figure 6. Gradient deviations. Top: Theoretical waveform for the application of two trapezoidal gradients with alternating sign. Middle: A comparison of the theoretical (dotted) and experimental positions in k-space reveals deviations best visualized in a corresponding difference plot (bottom). The flattened curve corresponds to the difference after modeling the gradient behavior with a linear system of second order.

reconstruction by regularization and estimation methods (19). However, even after the implementation of respective algorithms, the resulting image quality retained its pronounced sensitivity to changes of the inversion parameters. These observations require further investigations and at present certainly hamper the use of the BURS reconstruction for spiral imaging.

Summary

With respect to image reconstruction of spiral k-space acquisitions, conventional regridding with an analytical density compensation emerges as the most promising approach, as it offers fast and reliable processing of high-quality images. The simple augmented matrix method yields high speed for the regridding process, but suffers from residual image artifacts, and therefore may be a choice for experimental purposes only. At present, the general applicability of the BURS method seems to be limited because of a lack of robustness.

A number of further improvements to the gridding step have recently been suggested. For example, the combination of the augmented matrix method with iterative reconstructions may indeed have potential to enhance the achievable quality of (simulated) spiral images beyond the level demonstrated here. However, this work should be secondary to dealing with the experimental difficulties of the measurement process itself, discussed below.

SENSITIVITY TO ARTIFACTS

Figure 5 (top row) compares experimental FLASH, EPI, and spiral images of a standard quality assurance phantom obtained at 2.9 T. All experimental spiral images were based on gradient waveforms calculated by the Glover method (7) and image reconstruction by conventional regridding with analytical density compensation and twofold oversampling.

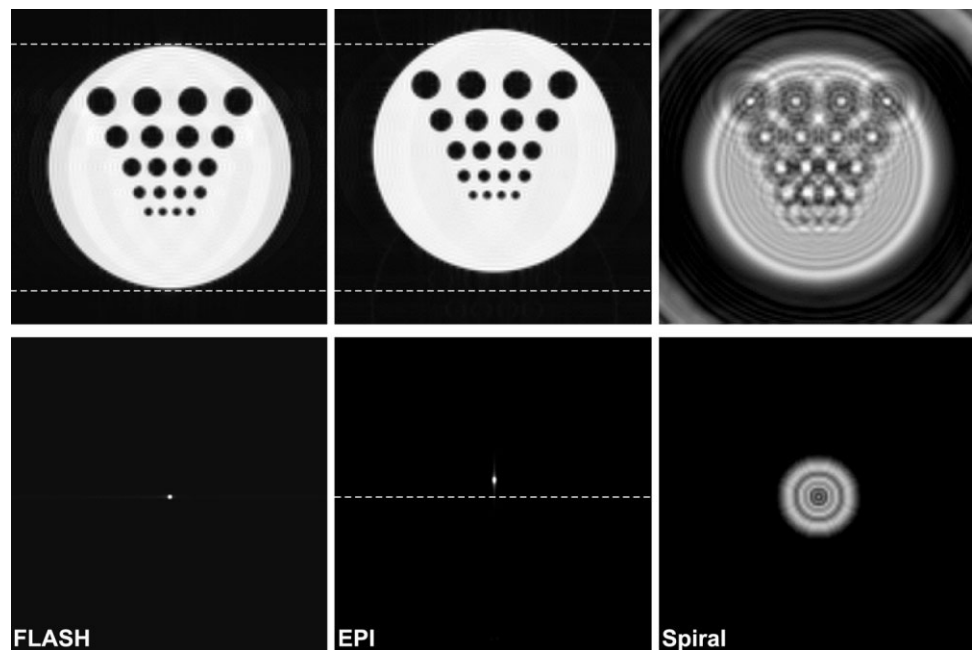


Figure 7. Off-resonance effects. Simulated images (top) and corresponding PSFs (bottom) for a FLASH, EPI, and spiral trajectory in the presence of a global phase drift.

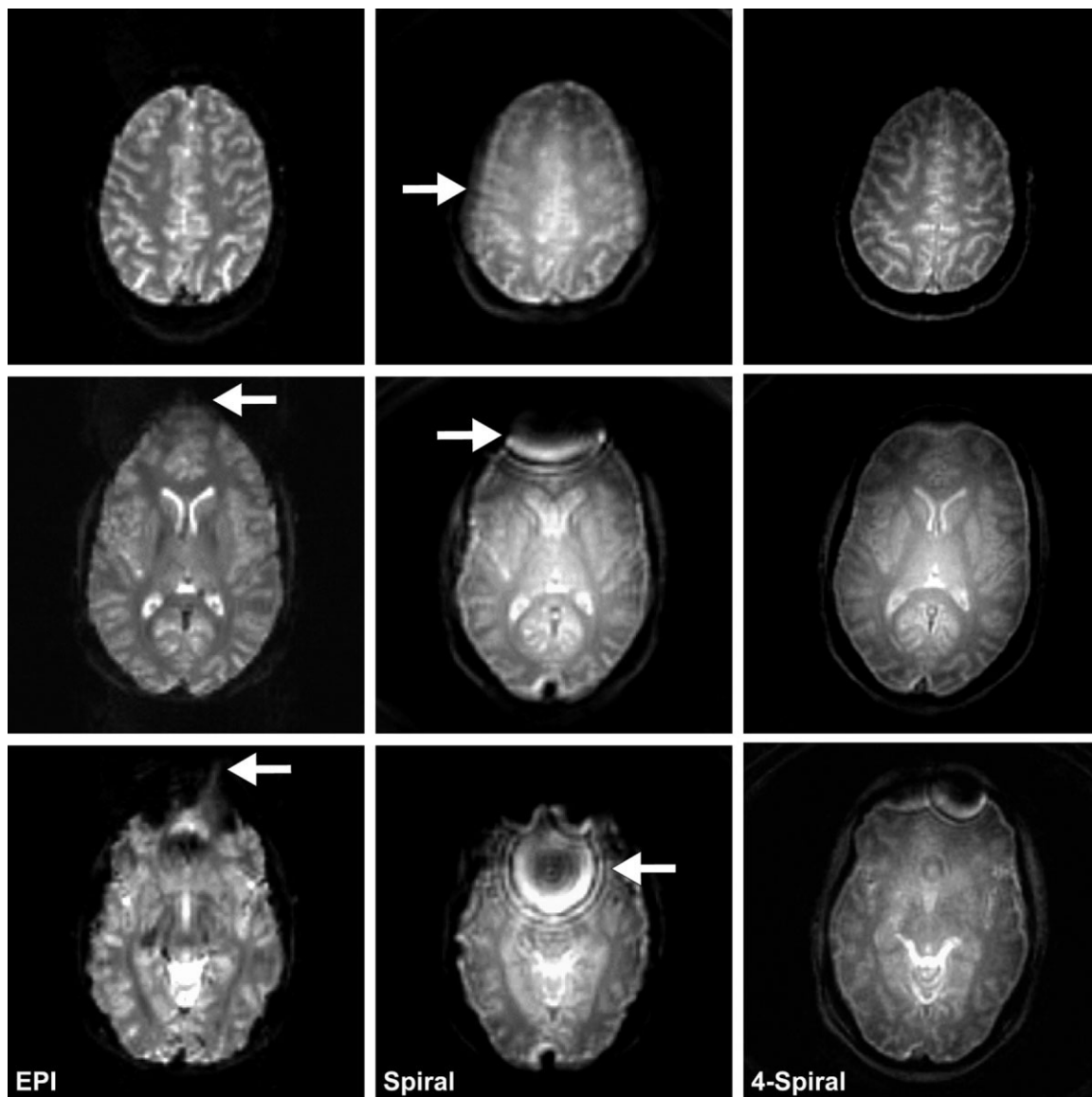


Figure 8. Experimental demonstration of off-resonance artifacts (arrows) in transverse images of the human brain at 2.9 T (three sections from top to bottom). One-dimensional geometric distortions in EPI (left) as opposed to pronounced two-dimensional blurring and extended ring-shaped artifacts in single-shot spiral imaging (middle). Right: Reduction of off-resonance artifacts by interleaved multishot spiral acquisitions with four excitations.

In comparison with FLASH imaging, EPI is affected by the well-known ghosting artifacts and geometric distortions as, for example, indicated by the curvature of the horizontal rows of circular spaces in the phantom. The EPI artifacts appear more pronounced than usual because at this stage—similar to the spiral acquisition—none of the corrections were applied that are normally employed to compensate for putative deviations of the actual trajectory from the theoretical trajectory used for image reconstruction. In the spiral image with the uncorrected trajectory, the object presents with intensity distortions such as a dark outer border. The image also appears both twisted and blurred, which strongly affects most of the circular spaces. The observed problems, or more precisely the underlying experimental sensitivities, are typical characteristics of EPI and spiral trajectories, and to a certain degree limit their prac-

tical utility. The following section attempts to identify the physical origins, which include imperfections of the gradients, off-resonance effects, and concomitant fields.

Gradient Deviations

In order to evaluate the influence of experimental deviations of the gradients from the theoretical waveforms, the temporal evolutions of the actually generated gradient fields were measured using an approach originally proposed by Duyn et al (20).

The results shown in Fig. 6 refer to a trapezoidal switch of a single gradient and indicate that in practice, deviations from the theoretical gradient field cannot be avoided. The occurrence of a damped response and gradient overshoot is best visualized in the difference

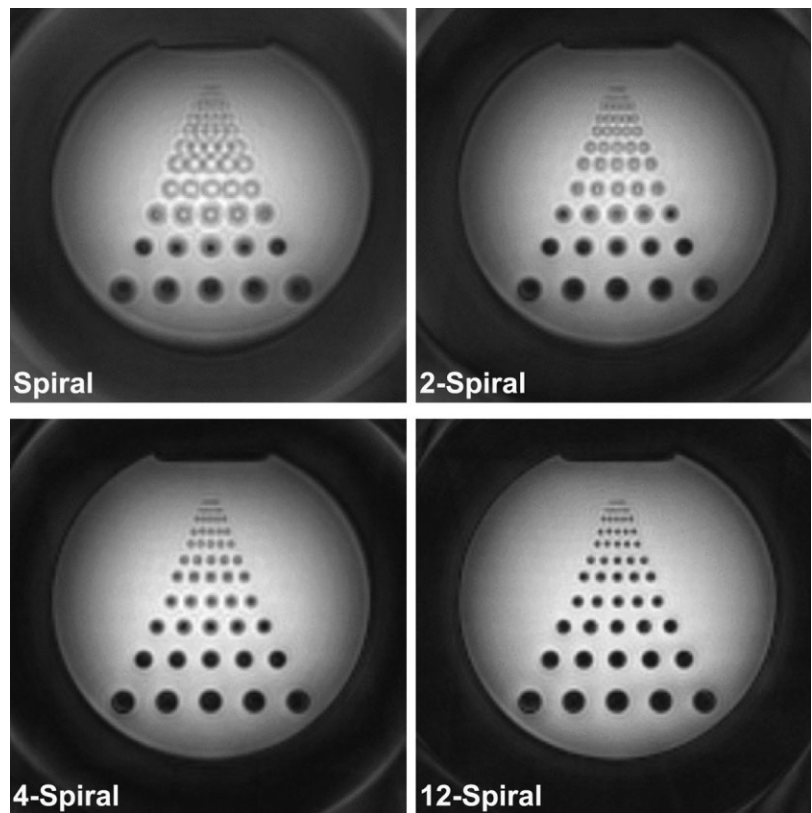


Figure 9. Experimental reduction of off-resonance blurring artifacts in single-shot spiral images (same phantom as in Fig. 5) by interleaved multishot spiral acquisitions with 2, 4, and 12 excitations (e.g., note the improved delineation of the circular spaces). All images were obtained under otherwise identical conditions, including the same spatial resolution.

plot. Because deviations occur in all three gradient orientations, the corresponding displacements of data points in k-space affect the image reconstruction when performed with the theoretical trajectory.

The impact of such deviations onto the image quality was simulated by assuming a driven linear system of second order for the actual gradient behavior. As demonstrated by the flattened curve in the difference plot of Fig. 6, the model offers a first-order approximation of the actual behavior. Realistic system parameters were estimated by fitting the simulated trajectory to the measured trajectory. The results of these simulations, which were performed by using the theoretical trajectory for reconstructing the data from the modeled (distorted) trajectory, are shown in Fig. 5 (middle row) for a numerical phantom similar to that employed in the experiments. A comparison of the resulting artifacts with those obtained experimentally in Fig. 5 (top row) identifies the nature of some of the distortions: ghosting in EPI as well as twisting and intensity distortions in spiral imaging can be largely attributed to the deviations of the gradients.

An often applied simple correction for the gradient deviations employs a slight shift of the trajectory in time. The method mainly compensates for the damped response behavior of the gradients. Although the corresponding experimental images in Fig. 5 (bottom row) are certainly improved, EPI still suffers from residual ghosts and geometric distortions, as evidenced by the curved rows of circular spaces. Most remarkably, however, the blurring of the circular spaces in the spiral image was not improved, and therefore has to be ascribed to a different physical process.

In EPI, a further improvement may be obtained using navigator scans together with a phase correction (21). Because this principle cannot be adapted to spiral imaging, it has been suggested to use the measured trajectory for the assignment of k-space positions for image reconstruction. In the present study, however, this approach failed by causing new artifacts. As this was especially true for spiral images at high spatial resolution, the successful use of a measured trajectory seems to depend on its signal-to-noise ratio and the ability to correctly monitor even small deviations. These findings suggest a pronounced sensitivity of the actual trajectory to the complex behavior of the gradient system. In general, the development of a robust correction method for experimental gradient deviations remains an open question for both EPI and spiral imaging.

Off-Resonance Effects

Off-resonance effects refer to signal contributions with resonance frequencies other than the central water proton resonance frequency used for RF irradiation (and signal reception). Such deviations may be caused by chemically shifted resonances such as lipid protons, inhomogeneities of the static magnetic field, susceptibility differences at air-tissue interfaces, and eddy currents. During the imaging process, i.e., between RF excitation and signal detection, off-resonance signals result in the accumulation of (local) phase errors and respective image artifacts.

In order to investigate the quantitative impact of off-resonance effects, the problem was modeled by introducing a global phase drift into the simulation process.

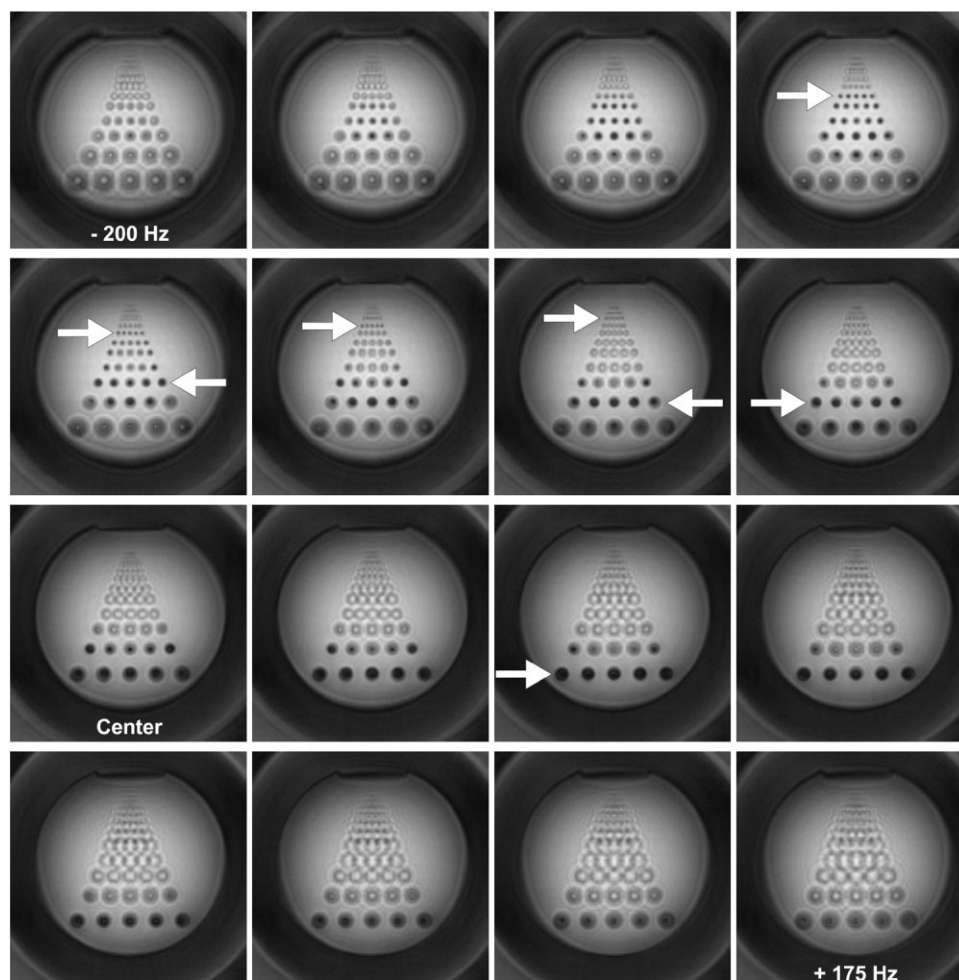


Figure 10. Experimental demonstration of off-resonance blurring artifacts in single-shot spiral images (same phantom as in Fig. 5) as a function of reconstruction frequency. From top left to bottom right, successive images vary by 25 Hz. Correct reconstructions of selected regions (circular spaces) in individual images are indicated by arrows.

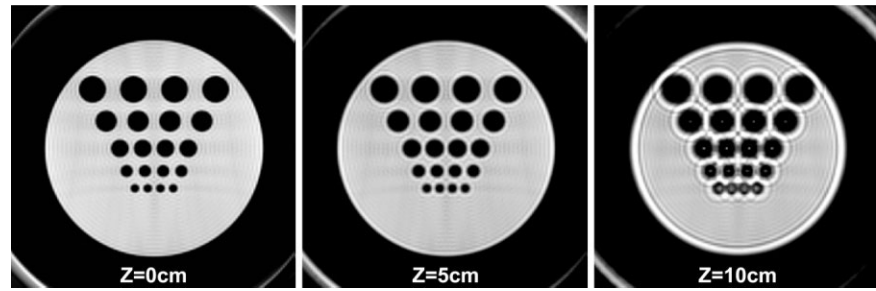
Figure 7 shows the simulated images and the corresponding point-spread function (PSF) for a FLASH, EPI, and spiral trajectory. While FLASH images remain unaffected, the phase drift causes a spatial shift in EPI along the phase-encoding dimension of the image. In spiral imaging, off-resonance effects cause pronounced (two-dimensional) blurring, which leads to a significant deterioration of the achievable image quality. The marked difference of FLASH and EPI trajectories vs. spiral trajectories is further documented by the extended ringing structure of the spiral PSF. This unpleasant behavior is also observed under in vivo conditions and represents a major threat to spiral imaging.

Figure 8 compares EPI and spiral acquisitions of the human brain in three transverse sections that are differently contaminated by off-resonance signal contributions from the sagittal sinus and nasal cavities. Apart from signal losses that are mainly caused by improperly refocused slice selection gradients, these well-known susceptibility effects cause locally varying (one-dimensional) displacements of image fragments in EPI (Fig. 8, left column) that lead to erroneous geometric representations along the phase-encoding dimension: here an artificial elongation of the anterior-posterior brain dimension. In single-shot spiral imaging (Fig. 8, central column), the same local phase errors lead to significantly larger blurring artifacts, with the ring structures already seen in Fig. 7.

There are two basic approaches to reduce off-resonance artifacts, which are similarly applicable to EPI and spiral trajectories: a shortening of the acquisition period and the use of postprocessing phase corrections. As demonstrated in vivo in Fig. 8 (right column) and more quantitatively for a phantom in Fig. 9, the only unambiguously successful strategy for spiral imaging is the use of interleaved multishot trajectories. In fact, the reduction (4-shot spirals, Figs. 8 and 9) or almost elimination (12-shot spiral, Fig. 9) of the severe ring-shaped artifacts in single-shot spiral images with increasing number of excitations again adds evidence to the off-resonance nature of this blurring problem. Noteworthy, all images shown in Fig. 9 possess the same spatial resolution.

Postprocessing phase corrections attempt to improve the off-resonance sensitivity of single-shot spirals. In principle, locally correct images may be obtained by image reconstruction with the proper local resonance frequency. Figure 10 shows several reconstructions of the same experimental data set as a function of frequency. As indicated by arrows, individual areas are accurately reconstructed without blurring if the chosen resonance frequency matches the respective off-resonance effect. Unfortunately, a reduction of off-resonance artifacts by a multifrequency reconstruction involves a large number of complex arithmetic operations, which renders the idea impractical for rou-

Figure 11. Concomitant field effects. Simulated transverse spiral images (same numerical phantom as in Fig. 7) as a function of off-center position. The concomitant field has been estimated using Eq. [6] for the conditions of the 2.9-T MRI system used here.



tine applications. Nevertheless, several approaches have been proposed to reduce the number of operations at the expense of accuracy (22–24). Regardless of technical considerations, a central problem of the multifrequency reconstruction is the selection of the right frequency for each image position. Typically, this information is achieved by field mapping using phase images with different echo times. However, field maps also pose problems as the identification of phase values exceeding 2π relies on phase unwrapping techniques with nontrivial algorithms (25,26). In addition, the frequency estimation from the field map fails for multiple phase wraps in areas of marked susceptibility differences, while putative subject movements may require frequent updates of the field map. In conclusion, a standardized and robust correction method for off-resonance effects in both single-shot EPI and spiral imaging is still missing, but urgently needed, as a prerequisite for reliable applications.

Concomitant Fields

A pure gradient field violates the Maxwell equation $\nabla \cdot \mathbf{B} = 0$. Hence, in MRI a deviation between the actually generated field and a pure gradient is always present. These additional fields are referred to as concomitant fields. They lead to phase errors that depend on position and gradient strength. Similar to the situation for off-resonance contributions, these phase errors cause geometric distortions in EPI and blurring in spiral imaging. The latter effect is demonstrated in Fig. 11 using simulations of transverse spiral images in the isocenter of the magnet as well as 5 and 10 cm off-center. Here, the ring-shaped artifacts of the circular spaces are quantitatively less pronounced, but otherwise identical to the off-resonance blurring depicted in Fig. 7.

In contrast to off-resonance effects, however, the phase error due to concomitant fields does not depend on the acquisition time. Therefore, it is not possible to assess its influence with the use of a field map. An approximate estimation of the problem may be derived using the second-order terms of the Taylor expansion of the magnetic field (27). Hence, the phase error from the concomitant field

is given by

$$\phi_c(t) = \gamma \int_0^t B_c(\tau) d\tau. \quad (6)$$

In order to determine the exigency of a correction mechanism, Eq. [6] serves to calculate the concomitant field effects for the experimental setup used here. Simulations of spiral acquisitions in the presence of respective fields revealed that a correction cannot be avoided. As shown in Fig. 11, this especially applies to single-shot spirals at distances to (or with image components at) about 10 cm from the isocenter. These findings are in line with results presented by King et al (28). Because the phase, except for transverse sections, varies within the image, the basic idea for a correction is to subtract the phase values estimated from Eq. [6] for every position in the image. Similar to the algorithms proposed for correcting off-resonance effects, suitable methods require a large number of operations (28), so that any practical implementation needs to develop a trade-off between computational performance and speed.

CONCLUSION

The numerical simulations presented here clearly demonstrate that spiral imaging faces no principle problems with respect to trajectory design and image reconstruction by density-corrected regridding. Although the procedures involve more elaborate algorithms and computational efforts than conventional scanning based on a rectangular sampling of k-space, the achievable image quality with existing methods is fully sufficient and not the determining factor for practical applications. In fact, a further possible refinement in these areas is not expected to lead to a significant improvement of experimentally acquired images. This is because spiral images are less tolerant to some of the unavoidable instrumental or in vivo inadequacies than EPI or even conventional gradient-echo imaging. In fact, the in vivo image artifacts caused by off-resonance effects due to susceptibility differences are often unacceptable, as they always present as an extended ring-shaped blurring of affected image fragments. Finally, it should be noted that the tight coupling of the encoding gradients in spiral imaging precludes both a straightforward use of partial Fourier sampling and an effective reduction of the acquisition time by a nonsquare FOV. Thus, improvements in image quality that are obtainable by re-

$$B_c(x, y, z) = \frac{G_x^2 + G_y^2}{2B_0} z^2 - \frac{G_z G_y}{2B_0} zy - \frac{G_z G_x}{2B_0} zx + \frac{G_z^2}{8B_0} x^2 + \frac{G_z^2}{8B_0} y^2 + O^3 \quad (5)$$

ducing the length of the acquisition period are only possible for a multishot scenario at the expense of the high-speed advantage or by adapting the principles of partially parallel imaging. Because the latter approach is also applicable to EPI, the present results suggest that spiral imaging may find specific applications, most likely in areas where its inherent flow-compensating properties may be exploited, while the general needs for high-speed imaging are more easily served by EPI.

ACKNOWLEDGMENT

The authors thank Dr. Oliver Natt for helpful discussions during preparation of the manuscript.

REFERENCES

1. Nishimura DG, Irarrazabal P, Meyer C. A velocity k-space analysis of flow effects in echo-planar and spiral imaging. *Magn Reson Med* 1995;33:549–556.
2. Glover GH, Lee AT. Motion artifacts in fMRI: comparison of 2DFT with PR and spiral scan methods. *Magn Reson Med* 1995;33:624–635.
3. Gatehouse PD, Firmin DN. Flow distortion and signal loss in spiral imaging. *Magn Reson Med* 1999;41:1023–1031.
4. Shepp LA, Logan BF. The Fourier reconstruction of a head section. *IEEE Trans Nucl Sci* 1974;21:21–43.
5. Börnert P, Schomberg H, Aldefeld B, Groen J. Improvements in spiral MR imaging. *MAGMA* 1999;9:29–41.
6. King KF, Foo TKF, Crawford CR. Optimized gradient waveforms for spiral scanning. *Magn Reson Med* 1995;34:156–160.
7. Glover HG. Simple analytic spiral k-space algorithm. *Magn Reson Med* 1999;42:412–415.
8. Oesterle C, Markl M, Strecker R, Kraemer FM, Hennig J. Spiral reconstruction by regridding to a large rectilinear matrix: a practical solution for routine systems. *J Magn Reson Imaging* 1999;10:84–92.
9. Moriguchi H, Duerk JL. Iterative next-neighbor regridding (INNG): improved reconstruction from nonuniformly sampled k-space data using rescaled matrices. *Magn Reson Med* 2004;51:343–352.
10. Youla DC, Webb H. Image restoration by the method of convex projections. Part 1: theory. *IEEE Trans Med Imaging* 1982;1:81–94.
11. Sezan MI, Stark H. Image restoration by the method of convex projections. Part 2: applications and numerical results. *IEEE Trans Med Imaging* 1982;1:95–101.
12. O'Sullivan JD. A fast sinc function gridding algorithm for Fourier inversion in computer tomography. *IEEE Trans Med Imaging* 1985;4:200–207.
13. Jackson J, Meyer CH, Nishimura DG, Macovski A. Selection of a convolution function for Fourier inversion using gridding. *IEEE Trans Med Imaging* 1991;10:473–478.
14. Meyer CH, Hu BS, Nishimura DG, Macovski A. Fast spiral coronary artery imaging. *Magn Reson Med* 1992;28:202–213.
15. Rasche V, Proksa R, Sinkus R, Börnert P, Eggers H. Resampling of data between arbitrary grids using convolution interpolation. *IEEE Trans Med Imaging* 1999;18:385–392.
16. Rosenfeld D. An optimal and efficient new gridding algorithm using singular value decomposition. *Magn Reson Med* 1997;40:14–23.
17. Press WH. Numerical recipes in c: the art of scientific computing, 2nd edition. Cambridge: Cambridge University Press; 2002. 994 p.
18. Moriguchi H, Duerk JL. Modified block uniform resampling (BURS) algorithm using truncated singular value decomposition: fast accurate gridding with noise and artifact reduction. *Magn Reson Med* 2001;46:1189–1201.
19. Rosenfeld D. New approach to gridding using regularization and estimation theory. *Magn Reson Med* 2002;48:193–202.
20. Duyn JH, Yang Y, Frank JA, van der Veen JW. Simple correction method for k-space trajectory deviations in MRI. *J Magn Reson* 1998;132:150–153.
21. Bruder H, Fischer H, Reinfelder HE, Schmitt F. Image reconstruction for echo planar imaging with nonequidistant k-space sampling. *Magn Reson Med* 1992;23:311–323.
22. Man L, Pauly JM, Macovski A. Multifrequency interpolation for fast off-resonance correction. *Magn Reson Med* 1997;37:785–792.
23. Noll DC. Reconstruction techniques for magnetic resonance imaging. PhD thesis, Stanford University, California, 1991.
24. Noll DC, Pauly JM, Meyer CH, Nishimura DG, Macovski A. Deblurring for non-2D Fourier transform magnetic resonance imaging. *Magn Reson Med* 1992;25:319–333.
25. Chavez S, Xiang Q, An L. Understanding phase maps in MRI: a new outline phase unwrapping method. *IEEE Trans Med Imaging* 2002;21:966–977.
26. Jenkinson M. Fast, automated, n-dimensional phase-unwrapping algorithm. *Magn Reson Med* 2003;49:193–197.
27. Du YP, Zhou XJ, Bernstein MA. Correction of concomitant magnetic field-induced image artifacts in nonaxial echo-planar imaging. *Magn Reson Med* 2002;48:509–515.
28. King KF, Ganin A, Zhou XJ, Bernstein MA. Concomitant gradient field effects in spiral scans. *Magn Reson Med* 1999;41:103–112.